

# Analytical modeling of side grinding of orthogonal laminated SiCf/SiC composites based on effective elastic properties

Zikang Zhang

Songmei Yuan ([✉ yuansmbuua@163.com](mailto:yuansmbuua@163.com))

Beihang University

Xiaoxing Gao

Weiwei Xu

Jiaqi Zhang

Wenzhao An

---

## Research Article

**Keywords:** Cutting force model, Effective elastic properties, Orthogonal laminated SiCf/SiC composites, Side grinding, Removal mechanism

**Posted Date:** February 11th, 2022

**DOI:** <https://doi.org/10.21203/rs.3.rs-1334945/v1>

**License:**  This work is licensed under a Creative Commons Attribution 4.0 International License.

[Read Full License](#)

---

# Abstract

$\text{SiC}_f/\text{SiC}$  composites have been applied in numerous fields because of their outstanding properties like high specific strength and high specific modulus. However, defects can be produced during grinding because the composites are hard and brittle. Moreover, the fabrication process of laminated  $\text{SiC}_f/\text{SiC}$  composites is complicated and unstable, resulting in large differences in their elastic properties. Therefore, the effective elastic properties of composites needs to be obtained through theoretical analysis. In this study, the anisotropy of orthogonal laminated  $\text{SiC}_f/\text{SiC}$  composites and the fracture removal mechanism of the brittle material were both considered to develop a more accurate model. The effective elastic constants of the laminated composites were calculated using a macromechanical analysis. The grinding process was divided into the ductile, ductile-to-brittle transition, and brittle stages for analysis by the critical cutting depth. The modeling development was based on the interaction between the diamond grains and workpiece. Substituting the effective elastic constants into the model, the predicted value is consistent well with the experimental value. The cutting force value presents a non-linear decreasing trend with increasing spindle speed but increases linearly with increasing feed rate and cutting width. The spindle speed and cutting width have more influence on the cutting force than the feed rate. Increasing the spindle speed and decreasing the feed rate and cutting width can reduce the cutting force. The model can be applied to adequately evaluate the effective elastic properties of laminated  $\text{SiC}_f/\text{SiC}$  composites and effectively improve the grinding processes and machining efficiency in future applications.

## 1. Introduction

Silicon carbide ( $\text{SiC}$ ) fibre reinforced  $\text{SiC}$  ceramic matrix composites ( $\text{SiC}_f/\text{SiC}$ ) are advanced materials with excellent physical-mechanical properties, such as low thermal expansion coefficient, low density, high tensile modulus, and high specific strength; as a result, they have been widely used in aerospace, rail transportation and other fields in recent years [1–3]. Unidirectional composites are composed of a matrix and fibres aligned in the same direction and are referred to as monolayer composites when their thickness is small [4]; unlike metal materials, laminated  $\text{SiC}_f/\text{SiC}$  composites are anisotropic. The forming technology of  $\text{SiC}_f/\text{SiC}$  composites is near-net-shape processing, and the composites require secondary processing to meet the high precision demand. Grinding is a common machining method for this material [5, 6]. However,  $\text{SiC}_f/\text{SiC}$  composites are prone to matrix cracking, fibre pull-out, and damage in the grinding process due to their hardness, brittleness, and heterogeneity [7], leading to low processing efficiency, tool wear, and numerous other problems [8, 9]. Therefore, an effective processing method of  $\text{SiC}_f/\text{SiC}$  composites should be developed to achieve the desired high efficiency and quality.

The cutting force is an important output variable of the grinding process, influencing the cutting temperature, machining accuracy, and surface integrity [10]. As the magnitude of the cutting force is closely related to the cutting speed, feed rate, cutting depth, and material properties, a cutting force model could be used to control the effective factors and reduce the material defects by predicting the cutting

force in the grinding process. Numerous investigations have been conducted on the grinding process of brittle materials. It is reported that the ductile-to-brittle transition of hard and brittle materials is not an instantaneous value but an intermediate stage [11–13]. According to the ground surface and subsurface morphology, cutting force, and specific cutting energy of brittle materials, the removal mechanisms are divided into the ductile, ductile-to-brittle transition, and brittle stages [14]. Moreover, the individual diamond grains are subjected to a normal cutting force perpendicular to the contact surface and a tangential cutting force in the direction of motion [15], increasing the tensile stresses and expanding the median cracks [16]. Cheng et al. [17] designed a series of scratching tests and developed a cutting force model, the critical cutting depth and forces of the ductile-to-brittle transition have been determined to distinguish the three cutting stages. Xiao et al. [18] and Kar et al. [19] took the consideration of the brittle fracture material removal mechanism and proposed a cutting force model of grinding ceramics, the trends of the predicted cutting forces are in good agreement with those of experimental results in their studies. Some scholars have focused on the modeling processing of composites in recent decades. Yin et al. [20] developed a dynamic cutting force model of  $\text{SiC}_p/\text{Al}$  composites based on analysing the mechanical mechanisms and the heat generation mechanisms. The model can accurately present the dynamic fluctuation characteristics of the cutting process of  $\text{SiC}_p/\text{Al}$  composites. For long fibre reinforced composites, Zhang et al. [21] developed a series of particular surface grinding experiments and established a cutting force model of unidirectional  $\text{C}_f/\text{SiC}$  composites based on multiple-exponential function method. The results show that the grinding parameters have a significant impact on the grinding force. Ning et al. [22] and Wang et al. [23] homogenized the monolayer carbon fiber reinforced plastic (CFRP) composites through microscopic analysis and developed a cutting force model. The model prediction agrees well with the experimental results under different groups of input variables in their studies. However, for laminated composites, the anisotropy between the layers should also be considered. Due to the complexity and instability of the preparation process of laminated composites, the elastic properties of laminated composites contain large differences. Therefore, the effective elastic properties should be determined through theoretical analysis to establish a more accurate cutting force model.

In summary, numerous investigations have been carried out on modeling of brittle and homogeneous materials. However, cutting force modeling of laminated composites, such as  $\text{SiC}_f/\text{SiC}$ , is not extensive. In this study, the anisotropy of laminated composites and the fracture removal mechanism of the brittle material were both considered to develop a more accurate model. The effective elastic properties of orthogonal laminated  $\text{SiC}_f/\text{SiC}$  composites were discussed considering anisotropy using a macromechanical analysis. The removal mechanisms are divided into three cutting stages based on the critical conditions for the ductile-brittle transition. Final cutting force model was verified by experiment. The cutting force model reveals the relationship between the interaction force and material removal process and provides important guidance for modeling of side grinding of orthogonal laminated  $\text{SiC}_f/\text{SiC}$  composites.

## 2. Material Analysis

## 2.1. Material preparation

$\text{SiC}_f/\text{SiC}$  is composed of SiC fibres ( $\text{SiC}_f$ ), an SiC matrix ( $\text{SiC}_m$ ), and their interface. In this experiment, the composites were prepared using a melt infiltration (MI) process. First, the interface was prepared on the fibre surface using a chemical vapour infiltration (CVI) process. Then, multiple bundles of fibres were converted into unidirectional bands, and the preforms were obtained by laminated hot pressing and high-temperature cracking. Finally, the preforms were siliconized to obtain the materials. The material parameters of  $\text{SiC}_f/\text{SiC}$  composites are shown in Table 1.

Table 1  
Material parameters of  $\text{SiC}_f/\text{SiC}$  composites.

| Item  | Value |
|---|-------|
| Diameter of $\text{SiC}_f$ (um)   | 10~14 |
| Thickness of monolayer composites (um)  | 200   |
| Volume fraction of $\text{SiC}_f$ (%)   | 42    |
| Volume fraction of $\text{SiC}_m$ (%)   | 46    |
| Density of $\text{SiC}_f$ (g/cm <sup>3</sup> )  | 2.5   |
| Density of $\text{SiC}_m$ (g/cm <sup>3</sup> )  | 2.2   |
| The orthogonal laminated $\text{SiC}_f/\text{SiC}$ composites present a two-dimensional (2D) structure as shown in Fig. 1(a). The structure of the monolayer $\text{SiC}_f/\text{SiC}$ composites is shown in Fig. 1(b). The direction along the fibres is longitudinal and represented by direction 1; the direction perpendicular to the fibres is transverse and represented by direction 2; the direction perpendicular to plane 1-2 is vertical and represented by direction 3. The dimension of the thickness direction (direction 3) can be considered much smaller than that of the other two directions. |       |

In the overall analysis, the matrix can be considered an isotropic material, and the fibre a transverse isotropic material. Then, the monolayer  $\text{SiC}_f/\text{SiC}$  composites can be regarded as isotropic materials in plane 1-2. The mechanical properties of  $\text{SiC}_f/\text{SiC}$  composites are shown in Table 2.

Table 2  
Mechanical properties of SiC<sub>f</sub>/SiC composites.

|                       | Matrix (SiC <sub>m</sub> ) | Fibre (SiC <sub>f</sub> ) |             |             |
|-----------------------|----------------------------|---------------------------|-------------|-------------|
| Elastic modulus (GPa) | $E_m$                      | $E_{f1}$                  | $E_{f2}$    | $E_{f3}$    |
|                       | 105                        | 198                       | 173         | 173         |
| Poisson's ratio       | $\nu_m$                    | $\nu_{f12}$               | $\nu_{f23}$ | $\nu_{f31}$ |
|                       | 0.28                       | 0.23                      | 0.25        | 0.25        |

For the presentation, subscript  $f$  represents the silicon carbide fibre, and subscript  $m$  represents the silicon carbide matrix. For example,  $E_{f1}$  represents the fibre elastic modulus in direction 1;  $\nu_{f12}$  represents the Poisson's ratio in direction 1 of the SiC<sub>f</sub> in plane 1-2. The longitudinal effective elastic properties  $E_1$  and transverse effective elastic properties  $E_2$  of monolayer SiC<sub>f</sub>/SiC composites can be obtained by the following equations [24]:

$$E_1 = E_{f1} V_f + E_m V_m$$

$$E_2 = \frac{E_m}{1 - \sqrt{V_f} \left( 1 - E_m / E_{f2} \right)}$$

(1)

## 2.2. Analysis of the effective elastic properties of orthogonal laminated SiC<sub>f</sub>/SiC composites

### 2.2.1. Assumptions in analyzing development

When analyzing the macroscopic properties of laminated composites, a monolayer composite is considered a macroscopic homogeneous material, whose elastic properties conform to Eq. (1). In addition, the interlaminar performance of monolayer composites should be considered. The following assumptions are made in the analysis of the effective elastic properties:

- Each monolayer composite has the same thickness.
- The connection between the layers does not contain gaps.
- Stress and strain are evenly distributed in the laminated SiC<sub>f</sub>/SiC composites.
- The material follows Hooke's law (linear elasticity).

### 2.2.2. Approaches in analyzing development

Assuming that the thickness of the laminated SiC<sub>f</sub>/SiC composite material is  $h$ , each layer has the same thickness of  $h_i$ , and the total number of layers of the material is  $N$ . The geometric centre of the material is selected as the origin  $O_m$ , and the relative coordinate system of the material ( $x_m$ - $y_m$ - $z_m$ ) is established to facilitate the analysis ,as shown in Fig. 2(a).

$$\left\{ \begin{array}{l} \sigma_{11} \\ \sigma_{22} \\ \sigma_{33} \\ \sigma_{23} \\ \sigma_{31} \\ \sigma_{12} \end{array} \right\} = \left[ \begin{array}{cccccc} C_{11} & C_{12} & C_{13} & C_{14} & C_{15} & C_{16} \\ C_{12} & C_{22} & C_{23} & C_{24} & C_{25} & C_{26} \\ C_{13} & C_{23} & C_{33} & C_{34} & C_{35} & C_{36} \\ C_{14} & C_{24} & C_{34} & C_{44} & C_{45} & C_{46} \\ C_{15} & C_{25} & C_{35} & C_{45} & C_{55} & C_{56} \\ C_{16} & C_{26} & C_{36} & C_{46} & C_{56} & C_{66} \end{array} \right] \left\{ \begin{array}{l} \varepsilon_{11} \\ \varepsilon_{22} \\ \varepsilon_{33} \\ 2\varepsilon_{23} \\ 2\varepsilon_{31} \\ 2\varepsilon_{12} \end{array} \right\}$$

(2)

where  $\sigma$  and  $\varepsilon$  are the stress components and strain components, respectively.  $C_{11}, C_{12}, \dots, C_{66}$  are the components of the stiffness matrix  $[C]$ .  $[C]=[S]^{-1}$ , and  $[S]$  is the compliance matrix.

The effective constitutive relations can be written as follows:

$$\sigma_{ij}^* = [C^{**}] \varepsilon_{kl}^*, \quad \varepsilon_{ij}^* = [S^{**}] \sigma_{kl}^*$$

(3)

where  $[C^{**}]$  are effective stiffness coefficients and  $[S^{**}]$  are effective compliant coefficients.  $\sigma^{* ij}$  and  $\varepsilon^{* ij}$  are the average stress and strain, respectively, which are defined by the following equation:

$$\begin{aligned} \sigma_{ij}^* &= \frac{1}{V} \int_V \sigma_{ij} dV \\ \varepsilon_{ij}^* &= \frac{1}{V} \int_V \varepsilon_{ij} dV \end{aligned}$$

(4)

As a monolayer composite is transversely isotropic, the compliance matrix can be expressed as follows:

$$[S] = [C]^{-1} = \begin{bmatrix} \frac{1}{E_1} & -\frac{\nu_{12}}{E_1} & -\frac{\nu_{12}}{E_1} & 0 & 0 & 0 \\ -\frac{\nu_{21}}{E_2} & \frac{1}{E_2} & -\frac{\nu_{23}}{E_2} & 0 & 0 & 0 \\ -\frac{\nu_{21}}{E_2} & -\frac{\nu_{23}}{E_2} & \frac{1}{E_2} & 0 & 0 & 0 \\ 0 & 0 & 0 & \frac{1}{G_{23}} & 0 & 0 \\ 0 & 0 & 0 & 0 & \frac{1}{G_{12}} & 0 \\ 0 & 0 & 0 & 0 & 0 & \frac{1}{G_{12}} \end{bmatrix}$$

(5)

where  $\nu_{12}$  and  $\nu_{23}$  are longitudinal and transverse Poisson's ratios of monolayer composites, respectively, and they can be expressed as follows:

$$\nu_{12} = \nu_{f12} V_f + \nu_m V_m$$

$$\nu_{23} = \nu_{f23} V_f + \nu_m V_m \left[ \frac{1 + \nu_m - \nu_{12} (E_m / E_1)}{1 - \nu_m^2 + \nu_m \nu_{12} (E_m / E_1)} \right]$$

(6)

$\nu_{21}$  is the ratio of the contraction strain to the tensile strain in direction 1 with unidirectional stretching along direction 2,  $\nu_{21} / E_2 = \nu_{12} / E_1$ ;  $G_{23}$  and  $G_{12}$  are the shear modulus in planes 2-3 and 1-2, respectively, which conform to the following relationship:

$$G_{23} = \frac{E_2}{2(1 + \nu_{23})}, G_{12} = \frac{E_1}{2(1 + \nu_{12})}$$

(7)

The constitutive relation of a monolayer composite conforms to Eq. (2), which can be written as follows [25]:

$$\begin{array}{c} \sigma_{33}^* \\ \sigma_{23}^* \\ \sigma_{31}^* \\ \sigma_{11} \\ \sigma_{22} \\ \sigma_{12} \end{array} = \begin{bmatrix} [A] & [B] \\ [B]^T & [D] \end{bmatrix} \begin{array}{c} \varepsilon_{33} \\ 2\varepsilon_{23} \\ 2\varepsilon_{31} \\ \varepsilon_{11}^* \\ \varepsilon_{22}^* \\ 2\varepsilon_{12}^* \end{array}$$

(8)

where  $[A]$ ,  $[B]$ , and  $[D]$  are given by the following equations:

$$[A] = \begin{bmatrix} C_{33} & C_{34} & C_{35} \\ C_{34} & C_{44} & C_{45} \\ C_{35} & C_{45} & C_{55} \end{bmatrix} \quad [B] = \begin{bmatrix} C_{13} & C_{23} & C_{36} \\ C_{14} & C_{24} & C_{46} \\ C_{15} & C_{25} & C_{56} \end{bmatrix} \quad [D] = \begin{bmatrix} C_{11} & C_{12} & C_{16} \\ C_{12} & C_{22} & C_{26} \\ C_{16} & C_{26} & C_{66} \end{bmatrix}$$

(9)

The effective constitutive relation of a monolayer composite conforms to Eq. (3), which can be written as follows:

$$\begin{array}{c} \sigma_{33}^* \\ \sigma_{23}^* \\ \sigma_{31}^* \\ \sigma_{11}^* \\ \sigma_{22}^* \\ \sigma_{12}^* \end{array} = \begin{bmatrix} [a]^{-1} & [a]^{-1}[b] \\ [b]^T[a]^{-1} & [b]^T[a]^{-1}[b] + [d] \end{bmatrix} \begin{array}{c} \varepsilon_{33}^* \\ 2\varepsilon_{23}^* \\ 2\varepsilon_{31}^* \\ \varepsilon_{11}^* \\ \varepsilon_{22}^* \\ 2\varepsilon_{12}^* \end{array}$$

(10)

where  $[a]$ ,  $[b]$ , and  $[d]$  are given by the following equations:

$$\begin{aligned}[a] &= \frac{1}{h} \sum_{k=1}^N \int_{z_m}^{z_{m-1}} [A]^{-1} dz \\[b] &= \frac{1}{h} \sum_{k=1}^N \int_{z_m}^{z_{m-1}} [A]^{-1} [B] dz \\[d] &= \frac{1}{h} \sum_{k=1}^N \int_{z_m}^{z_{m-1}} \left( [D] - [B]^T [A]^{-1} [B] \right) dz\end{aligned}$$

(11)

Therefore, the effective compliance matrix of laminated SiC<sub>f</sub>/SiC composites can be expressed as follows [26]:

$$\left[ S^{**} \right] = \left[ C^{**} \right]^{-1} = \begin{bmatrix} S_{11}^{**} & S_{12}^{**} & S_{13}^{**} & S_{14}^{**} & S_{15}^{**} & S_{16}^{**} \\ S_{21}^{**} & S_{22}^{**} & S_{23}^{**} & S_{24}^{**} & S_{25}^{**} & S_{26}^{**} \\ S_{31}^{**} & S_{32}^{**} & S_{33}^{**} & S_{34}^{**} & S_{35}^{**} & S_{36}^{**} \\ S_{41}^{**} & S_{42}^{**} & S_{43}^{**} & S_{44}^{**} & S_{45}^{**} & S_{46}^{**} \\ S_{51}^{**} & S_{52}^{**} & S_{53}^{**} & S_{54}^{**} & S_{55}^{**} & S_{56}^{**} \\ S_{61}^{**} & S_{62}^{**} & S_{63}^{**} & S_{64}^{**} & S_{65}^{**} & S_{66}^{**} \end{bmatrix} = [a] - [b][d]^{-1}[b]^T$$

(12)

According to the relationship between the effective compliant coefficients and effective elastic properties, the effective elastic constants of laminated SiC<sub>f</sub>/SiC composites can be obtained by the following equations:

$$E_x = \frac{1}{S_{11}^{**}} \quad E_y = \frac{1}{S_{22}^{**}} \quad v_{xy} = -\frac{S_{12}^{**}}{S_{11}^{**}}$$

(13)

Finally, the effective elastic constants of the laminated SiC<sub>f</sub>/SiC composites are obtained as  $E_e = E_x \approx E_y = 134.24$  Gpa,  $v_e = v_{xy} = 0.26$ . These constants are used for the modeling shown in Section 3.

### 3. Development Of The Cutting Force Model

#### 3.1. Analysis of the cutting state of the grinding tool and workpiece

The grinding process in the tool-workpiece system can be considered as the combination of the cutting action of the whole diamond grains. A clear understanding of the interaction between the diamond grains and workpiece can be obtained by analyzing the cutting state and dynamic trajectory of a single diamond.

The schematic diagram of side grinding is shown in Fig. 3(a). The directions of feeding, cutting, and the tool axis are set as the  $x$ -axis,  $y$ -axis, and  $z$ -axis, respectively.  $F_x$  and  $F_y$  are the average forces measured by the dynamometer in the  $x$  and  $y$  directions in the grinding process, respectively;  $F_m$  is the combined force of these two forces used to evaluate the cutting forces in the entire grinding process;  $v_f$  is the feed rate of the tool, mm/s;  $\omega$  is the angular velocity of the spindle, rad/s.  $\omega = 2\pi n$ , and  $n$  is the spindle rotation speed, r/min. The thickness of the workpiece is denoted as  $h_m$ , mm. The diamond grains are considered octahedrons to simplify the modelling, as shown in Fig. 3(b).  $\theta$  is the semi-angle between two opposite edge of the diamond grains.  $S_a$  is the edge length of the diamond grains.

However, the diamond grains on the tool are randomly distributed, and the protruding height is not uniform, as shown in Fig. 4(a).  $O$  represents the tool center, and  $R_t$  is the radius of the tool substrate. The random protrusion height of diamond grains is  $\delta_{gi}$ . Fig. 4(b) shows the plane expansion of the diamond grains on the tool surface. The grain height is distributed around the average height. Therefore, the probability density function is required to describe the random protruding height characteristics of the diamond grains to better analyse the interaction between the diamond grains and workpiece and conveniently establish the cutting force model. The protruding height of diamond grains on the tool surface conforms to Rayleigh distribution [3]:

$$f(\delta_{gi}) = \{ \left( \delta_{gi} / \beta^2 \right) e^{-\left( \delta_{gi}^2 / 2\beta^2 \right)}, \delta_{gi} \geq 0 \}$$

(14)

where  $\beta$  is parameter defined by the probability density function.

The average protrusion height of diamond grains is  $\delta_{ga}$ , as shown in Fig. 4(c).  $R_a$  is the average tool radius used to calculate the diamond grains trajectory.  $R_a = R_t + \delta_{ga}$ ;  $\delta_{ga}$  can be determined by the expectation of the Rayleigh function. According to the probability statistics method, the expected and variance can be obtained by the following equations:

$$\begin{aligned} \left. \begin{aligned} E \left( \delta_{gi} \right) &= \beta \sqrt{\frac{\pi}{2}} \approx 0.253 \\ \left. \delta_{gi} \right) &\approx 0.429 \beta^2 \end{aligned} \right\} \end{aligned}$$

(15)

Substituting Eq. (14) into Eq. (15), it is given as follows:

$$E \left( \delta_{gi}^2 \right) = \left[ e^{-\delta_{gi}^2 / 2\beta^2} - \left( 1 - 2\beta^2 \right) \right]_0^\infty = 2\beta^2$$

(16)

The total removal volume of all diamond grains should be equal to the removal volume of the grinding process, which can be expressed as follows:

$$E \left( \delta_{gi}^2 \right) = \frac{2a_e v_f}{\pi C_e l_c v_s}$$

(17)

where  $C_e$  is the number of active diamond grains per square millimetre,  $C_e = 5$  in this paper;  $v_s$  is the cutting speed of a single diamond grain, mm/s;  $a_e$  is the cutting width, mm;  $l_c$  is grinding tool/workpiece arc length of contact, which can be expressed as follows:

$$l_c = \sqrt{2R_a \cdot a_e}$$

(18)

Therefore,  $\delta_{ga}$  can be obtained by the following expression:

$$\delta_{ga} = \sqrt{\frac{2a_e v_f}{\pi C_e l_c v_s}}$$

(19)

As shown in Fig. 4(d), after the average of the random protruding height, the randomly distributed diamond grains on the tool have a uniform height, consistent with the height of the average height plane, thus simplifying the grinding behaviour generated by the random protruding height, beneficial to the complete description of the processed surface.

The cutting mechanism of a single diamond grain is shown in Fig. 5(a1). Based on research on indentation and scratch experiments of hard and brittle materials, there are three cutting stages with a gradual increase of the normal cutting force  $F_n$  of a single diamond grain: ductile stage (stage I), ductile-to-brittle transition stage (stage II), and brittle stage (stage III). The normal and tangential cutting forces

are represented by  $F_n$  and  $F_t$  respectively.  $F_p$  is the resultant of these two forces, the theoretical cutting force, as shown in Fig. 5(a2).

According to the definition of Vickers hardness, the normal cutting force can be obtained by the following equation [27]:

$$\{F_n\} = \xi H a^2$$

(20)

where  $\xi$  is the geometrical factor of the indenter,  $\xi \approx 1.885$ ;  $H$  denotes Vickers hardness, which is 20 GPa;  $a$  denotes the indentation size,  $a = h_g \tan \theta$ , where  $h_g$  is the cutting depth of a single diamond grain.

Therefore, the three cutting stages depend on  $h_g$ , influencing the local contact deformation and material removal mechanism.

When  $0 < h_{g1} < h_{gp}$ , the cutting stage is the ductile stage (stage I), as shown in Fig. 5(b1). Here, the contact area between the diamond grain and workpiece is mainly the plastic deformation area caused by the pressure of the diamond grain, and no obvious cracks are present. Therefore, the materials are removed through plastic flow, and the tangential direction of the diamond grain is mainly affected by the rubbing force. The critical state of the ductile-brittle transition refers to the state in which the crack generated by the last diamond grain is immediately removed by the next grain. The critical depth can be expressed as follows [28]:

$$\{h_{gp}\} = \tau \{h_{gc}\}$$

(21)

where  $h_{gp}$  is the critical depth between stage I and stage II;  $h_{gc}$  is the critical depth between stage II and stage III;  $\tau$  is coefficients of the ductile stage, which is 0.25 in this paper.

When  $h_{gp} < h_{g2} < h_{go}$ , the cutting stage is the ductile-brittle transition stage (stage II), as shown in Fig. 5(b2). At this stage, the plastic zone beneath the diamond gradually expands. The median crack begins to appear beneath the plastic zone, which is usually related to strength degradation. The median crack occurs in the loading and unloading process. Unloading and tool wear result in uneven local stress distribution along the grinding path, and lateral cracks occurred during unloading. The residual stress component is the main source of crack propagation, and the tangential direction of the diamond grain is mainly subjected to ploughing force. The critical depth between stage II and stage III is related to the material properties, which can be expressed as follows [12]:

$$h_{gc}^* = \psi \left( T \right) \left( \frac{E_e}{H} \right)^2 \left( \frac{K_{IC}}{H} \right)^2$$

(22)

where  $K_{IC}$  is the static fracture toughness of the material, which is  $15.5 \text{ MPa/m}^{1/2}$ ;  $\psi(T)$  is a function of temperature, which is given as follows:

$$\psi(T) = 0.52 + 0.85 \exp(-T/T_0) \quad (23)$$

$T_0 = 251.1^\circ\text{C}$

where  $T$  is ambient temperature,  $^\circ\text{C}$ .

However, based on previous reports, using static fracture toughness in dynamic processing is not appropriate. The dynamic fracture toughness  $K_{ID}$  is approximately 30% of  $K_{IC}$  [29]. Therefore, substituting  $K_{ID}$  for  $K_{IC}$  can better conform to the actual grinding process and provide more accurate theoretical guidance for modeling, and the critical depth  $h_{gc}$  can be written as follows:

$$h_{gc} = \psi(T) \left( \frac{E_e}{H} \right) \left( \frac{K_{ID}}{H} \right)^2 \quad (24)$$

When  $h_{gc} < h_{g3}$ , the cutting stage is the brittle transition stage (stage III), as shown in Fig. 5(b3). At this stage, the plastic zone beneath the diamond grain expands further. Continuous crack branches occur beneath the plastic zone, and obvious transverse cracks occur in the workpiece and extend to the ground surface, resulting in material detritus and a large amount of removal. The diamond grains are subjected to tangential and normal loads. The tangential cutting force causes expansion of transverse cracks, reducing the surface quality of the workpiece and improving the removal rate. The lengths of the median crack, lateral crack, and plastic zone, denoted as  $C_m$ ,  $C_l$  and  $C_h$ , respectively, can be expressed as follows [30]:

$$\begin{aligned} C_m &= \eta_1 \left( \frac{\chi_e}{\chi_r} \right)^{1/3} \left( \frac{F_{t3}}{K_{ID}} \right)^{1/3} \cos^{4/9} \theta \\ C_l &= \eta_2 \cot^{5/12} \theta \left[ \frac{E_e}{H K_{ID}} \right]^{1/2} \left( 1 - \frac{\epsilon^2}{\eta_3} \right)^{1/2} F_{n3}^{5/8} \\ C_h &= \eta_3 \cot^{1/3} \theta \left[ \frac{E_e}{H F_{n3}} \right]^{1/2} \end{aligned} \quad (25)$$

where  $\chi_e$  and  $\chi_r$  are the indentation coefficients of the elastic stress field and residual stress field, respectively ( $\chi_e = 0.032$ ,  $\chi_r = 0.026$ );  $\eta_1$ ,  $\eta_2$  and  $\eta_3$  are the dimensional constants ( $\eta_1 = 0.0366$ ,  $\eta_2 = \eta_3 = 0.226$ ).

The cutting depth increases gradually from the time when a single diamond grain touches the workpiece to when it is removed. The maximum undeformed chip thickness  $h_{gm}$  can be obtained by the following expression [31]:

$$\{h_{gm}\}=2\{\delta_{ga}\}\left(\frac{\{a_e\}}{\{2R_a\}}\right)^{1/4}\sqrt{\frac{\{v_f\}}{\{v_s\}\{\eta_c\}f}}\left(\frac{4\pi}{3}\{V_d\}\right)^{2/3}$$

(26)

where  $\eta_c$  is the ratio of chip width to average undeformed chip thickness,  $\eta_c = 10$ ;  $f$  is the fraction of diamond grains that actively cut during grinding,  $f = 0.5$ ; The grinding tool used in this study has a concentration of 100 or volume fraction of  $V_d = 0.25$ .

## 3.2. Modeling development assumptions

The tangential and normal forces of a single diamond, decided by the dynamic trajectory and average cutting depth of a single diamond in the grinding process, are analysed to establish the cutting force model with the following assumptions and simplifications:

- (1) The diamond grains are perfectly bonded to the tool and will not fall off during grinding.
- (2) The diamond grains are octahedrons of the same size and the semi-angle  $\theta$  is  $60^\circ$ .
- (3) The experimental system keeps stable during grinding process.
- (4) The material deformation during the grinding process conforms to Hooke's law.

## 3.3. Cutting force model of a single diamond grain under three cutting stages

### 3.3.1. Kinematical analysis of a single diamond grain

The dynamic trajectory of a single diamond grain was analysed dynamically to clarify the side grinding process, and its position can be expressed by machining parameters. The three cutting stages of the ground region from  $A$  to  $A'$  is shown in Fig. 6. The position and velocity of a single diamond grain in the grinding process can be expressed as follows:

$$\begin{aligned} & \left. \begin{array}{l} x = R_a \sin(2\pi nt + v_f t) \\ y = R_a \cos(2\pi nt) \\ z = 0 \end{array} \right\} \\ & \left. \begin{array}{l} v_x = 2\pi n R_a \cos(2\pi nt + v_f t) \\ v_y = -2\pi n R_a \sin(2\pi nt) \\ v_z = 0 \end{array} \right\} \end{aligned}$$

(27)

where  $t$  is the cutting time, s.

The moment when a single diamond grain touches the workpiece is  $t_0$ ,  $t_0=0$  for convenience. At stage I, the tool center moves from  $O$  to  $O_1$ , and the corresponding cutting time is  $t_0-t_1$ . The corresponding cutting time is  $t_1-t_2$  and  $t_2-t_3$  when the tool center moves from  $O_1$  to  $O_2$  at stage II and from  $O_2$  to  $O_3$  at stage III,

respectively. The cutting lengths of a single diamond grain during the grinding process can be expressed as follows:

$$\begin{aligned} \text{\&begin\{gathered}} & \{l_1\}=\int_{t_0}^{t_1} \sqrt{v_x^2+v_y^2+v_z^2} dt \text{\&hfill} \\ & \{l_2\}=\int_{t_1}^{t_2} \sqrt{v_x^2+v_y^2+v_z^2} dt \text{\&hfill} \\ & \{l_3\}=\int_{t_2}^{t_3} \sqrt{v_x^2+v_y^2+v_z^2} dt \text{\&hfill} \end{gathered} \text{\&end\{gathered}}$$

(28)

where  $l_1$ ,  $l_2$ , and  $l_3$  are the cutting lengths at stage I, stage II, and stage III, respectively.

The feeding distance and cutting time of a single diamond grain can be obtained by the following expression:

$$\begin{aligned} \begin{array}{*{20}{c}} & \{x_1\}=\{v_f\}\{t_1\} & \& \{x_2\}=\{v_f\}\{t_2\} & \& \{x_3\}=\{v_f\}\{t_3\} \\ & \{\gamma_1\}=\omega\{t_1\} & \& \{\gamma_2\}=\omega\{t_2\} & \& \{\gamma_3\}=\omega\{t_3\} \\ & \{t_1\}=\frac{\{h_{gp}\}}{\{\{v_f\}\sin\{\gamma_1\}\}} & \& \{t_2\}=\frac{\{h_{gc}\}}{\{\{v_f\}\sin\{\gamma_2\}\}} & \& \{t_3\}=\frac{\{h_{gm}\}}{\{\{v_f\}\sin\{\gamma_3\}\}} \end{array} \end{aligned}$$

(29)

where  $x_1$ ,  $x_2$ , and  $x_3$  are the feeding distance at stage I, stage II, and stage III, respectively.  $\gamma_1$ ,  $\gamma_2$ , and  $\gamma_3$  are the rotation angle of the tool and the corresponding cutting time.

### 3.3.2. Cutting force model of a single diamond grain at the ductile stage

As the cutting depth  $h_{g1}$  of a single diamond grain is constantly changing with time at the ductile stage, the average cutting depth needs to be determined. The material removal volume of a single diamond grain at stage I, denoted as  $V_{g1}$ , can be considered as a triangular pyramid volume with the following expression:

$$V_{g1}=\frac{1}{3}l_1 \times h_{gp} \times h_{gp} \tan \theta = \frac{1}{3}l_1 h_{gp}^2 \tan \theta$$

(30)

The equivalent removal volume of a single diamond grain at the ductile stage can be idealized as a triangular prism, denoted as  $V_{ga1}$  with the following expression:

$$V_{ga1}=l_1 \times h_{ga1} \times h_{ga1} \tan \theta = l_1 h_{ga1}^2 \tan \theta$$

(31)

Then  $V_{g1} = V_{ga1}$ , and the average cutting depth at stage I, denoted as  $h_{ga1}$ , can be expressed as follows:

$$\{h_{ga1}\} = \frac{\sqrt{3}}{3} \{h_{gp}\}$$

(32)

The connection between the average normal cutting force  $F_{n1}$  and average cutting depth  $h_{ga1}$  at stage I can be expressed as follows [32]:

$$\{F_{n1}\} = 2Hh_{ga1}^2 \tan \theta \left( 2 + (\tan \theta)^2 \right)^{1/2}$$

(33)

Substituting Eqs. (21) and (32) into Eq. (33), the average normal cutting force  $F_{n1}$  can be expressed as follows:

$$\{F_{n1}\} = \frac{Hh_{gc}^2 \tan \theta}{2} \left( 2 + (\tan \theta)^2 \right)^{1/2}$$

(34)

At stage I, plastic deformation of the workpiece begins at yield criterion point with the increase of cutting depth, and the single diamond grain is mainly subjected to the rubbing force  $F_{t1}$  in the tangential direction, which can be expressed as follows:

$$\{F_{t1}\} = \mu \{F_{n1}\}$$

(35)

where  $\mu$  is the friction coefficient.

The friction coefficient of the diamond grain can be approximated to the ratio of the projected areas in the cutting and tangential directions [33], which is given as follows:

$$\mu = \frac{\{S_{t1}\}}{\{S_{n1}\}}$$

(36)

where  $S_{t1}$  and  $S_{n1}$  are the tangential and normal projection areas of the diamond grain at stage I, respectively, and they can be expressed as follows:

$$\begin{gathered} \{S_{t1}\} = \frac{1}{2} \times 2 \times \{h_{g1}\} \tan \theta \times \{h_{g1}\} = \{h_{g1}\}^2 \tan \theta \\ \{S_{n1}\} = \left( \sqrt{2} \times \{h_{g1}\} \tan \theta \right)^2 = 2 \{h_{g1}\}^2 (\tan \theta)^2 \end{gathered}$$

(37)

Substituting Eqs. (35), (36) and (37) into Eq. (34), the average rubbing force  $F_{t1}$  can be expressed as follows:

$$\{F_{\{t1\}}=\frac{\{Hh_{\{gc\}}\}^2\tan \theta}{\left(2+\{\tan \theta\}^2\right)^{1/2}}\}\{(48)\}$$

(38)

Finally, the total average cutting force at the ductile stage can be expressed as follows:

$$\{F_1=\sqrt{F_{\{n1\}}^2+F_{\{t1\}}^2}\}\text{ (48)}$$

(39)

### 3.3.3. Cutting force model of a single diamond grain at the ductile-brittle transition stage

The material removal volume of the single diamond grain at stage II, denoted as  $V_{g2}$ , can be obtained by the following expression:

$$\{V_{\{g2\}}=\frac{1}{3}\left(\{l_1+l_2\}\right)\times h_{\{gc\}}\times h_{\{gc\}}\tan \theta - \frac{1}{3}\{l_1\}\times h_{\{gp\}}\times h_{\{gp\}}\tan \theta\}$$

(40)

The removed volume of this stage is equivalent to the volume of the triangular prism, denoted as  $V_{ga2}$ , can be expressed as follows:

$$\{V_{\{ga2\}}=l_2 \times h_{\{ga2\}} \times h_{\{ga2\}}\tan \theta = l_2 h_{\{ga2\}}^2 \tan \theta\}$$

(41)

Then  $V_{g2} = V_{ga2}$ , and the average cutting depth at stage II, denoted as  $h_{ga2}$ , can be expressed as follows:

$$\{h_{\{ga2\}}=h_{\{gc\}}\left(\frac{15l_1+16l_2}{48l_2}\right)^{1/2}\}$$

(42)

Under the same normal load, the crack depth of multiple diamond grinding is approximately half of that of single diamond grinding. The connection between the average normal cutting force  $F_{n2}$  and average cutting depth  $h_{ga2}$  at stage II can be expressed as follows [18]:

$$\{F_{\{n2\}}=\frac{1}{2}\chi Hh_{\{ga2\}}^2\tan ^2\theta\}$$

(43)

Substituting Eq. (42) into Eq. (43), the average normal cutting force  $F_{n2}$  can be expressed as follows:

$$\{F_{n2}\} = \frac{1}{2} \xi H h_{gc}^2 \left( \frac{15l_1 + 16l_2}{48l_2} \right) \tan^2 \theta \quad (44)$$

The single diamond grain is mainly subjected to the ploughing force  $F_{t2}$  in the tangential direction at this stage, which can be expressed as follows:

$$\{F_{t2}\} = \sigma_s S_{t2} \quad (45)$$

where  $\sigma_s$  is the compressive yield stress at the contact area, which is defined as follows [34]:

$$\{\sigma_s\} = \left( \frac{H^4}{E_e} \right)^{1/3} \quad (46)$$

and  $S_{t2}$  is the projected area of the tangential direction of the diamond grain, which is related to the cutting depth. The projected area can be calculated by the average cutting depth as follows:

$$S_{t2} = \frac{1}{2} \times 2h_{ga2} \tan \theta \times h_{ga2} = h_{ga2}^2 \tan \theta \quad (47)$$

Substituting Eqs. (42), (46), and (47) into Eq. (45), the average ploughing force can be expressed as follows:

$$\{F_{t2}\} = \frac{h_{gc}^2}{2} \left( 15l_1 + 16l_2 \right) \tan \theta \left( \frac{H^4}{E_e} \right)^{1/3} \quad (48)$$

Finally, the total average cutting force at the ductile-brittle transition stage is given as follows:

$$F_2 = \sqrt{F_{n2}^2 + F_{t2}^2} = \sqrt{\frac{h_{gc}^2}{4} \left( 15l_1 + 16l_2 \right)^2 \tan^2 \theta + \left( \frac{h_{gc}^2}{2} \left( 15l_1 + 16l_2 \right) \tan \theta \left( \frac{H^4}{E_e} \right)^{1/3} \right)^2} \quad (49)$$

### 3.3.4. Cutting force model of a single diamond grain at the brittle stage

The material removal volume of the single diamond grain at stage III, denoted as  $V_{g3}$ , can be obtained by the following expression:

$$\{V_{g3}\} = \frac{1}{3} l_c \times h_{gm} \times h_{gm} \tan \theta - \frac{1}{3} \left( l_1 + l_2 \right) \right) \times h_{gc} \times h_{gc} \tan \theta$$

(50)

The removed volume of this stage is equivalent to the volume of the triangular prism, denoted as  $V_{ga3}$ , can be expressed as follows:

$$\{V_{ga3}\} = l_3 \times h_{ga3} \times h_{ga3} \tan \theta = l_3 h_{ga3}^2 \tan \theta$$

(51)

Then  $V_{g3} = V_{ga3}$ , and the average cutting depth at stage III, denoted as  $h_{ga3}$ , can be expressed as follows:

$$h_{ga3} = \sqrt{\left( \frac{h_{gm}^2 l_c - h_{gc}^2 \left( l_1 + l_2 \right)}{3 l_3} \right)^2 + \left( \frac{3 l_3}{2} \right)^2}$$

(52)

The average normal cutting force  $F_{n3}$  and tangential cutting force  $F_{t3}$  of a single diamond grain at stage III can be obtained by the following expression [35]:

$$\begin{aligned} F_{n3} &= \frac{1}{2} \eta_2 h_{ga3}^2 H^2 \tan^{8/3} \theta \left[ \frac{3}{\pi} \left( 1 - 2 \epsilon_e \right) \left( 5 - 4 \epsilon_e \right) + \frac{2 \sqrt{3} \cot \theta}{\pi} \left( 5 - 4 \epsilon_e \right) \sigma_s \right] \\ F_{t3} &= \frac{1}{2} \eta_2 C_h h_{ga3}^2 H^2 \tan^{8/3} \theta \left[ \frac{3}{\pi} \left( 1 - 2 \epsilon_e \right) \left( 5 - 4 \epsilon_e \right) + \frac{2 \sqrt{3} \cot \theta}{\pi} \left( 5 - 4 \epsilon_e \right) \sigma_s \right] \end{aligned}$$

(53)

The total average cutting force at the brittle stage can be expressed as follows:

$$F_3 = \sqrt{F_{n3}^2 + F_{t3}^2}$$

(54)

Substituting Eqs. (52) and (53) into Eq. (54), the total average cutting force  $F_3$  is given as follows:

$$F_3 = \sqrt{\left( \frac{3 \eta_2 l_3 C_h H^2 \tan^{8/3} \theta}{\pi} \left[ \left( 1 - 2 \epsilon_e \right) \left( 5 - 4 \epsilon_e \right) + \frac{2 \sqrt{3} \cot \theta}{\pi} \left( 5 - 4 \epsilon_e \right) \sigma_s \right] \right)^2 + \left( \frac{3 \eta_2 l_3 C_h H^2 \tan^{8/3} \theta}{\pi} \left[ \left( 1 - 2 \epsilon_e \right) \left( 5 - 4 \epsilon_e \right) + \frac{2 \sqrt{3} \cot \theta}{\pi} \left( 5 - 4 \epsilon_e \right) \sigma_s \right] \right)^2}$$

(55)

### 3.4. Final cutting force model of side grinding of orthogonal laminated SiC<sub>f</sub>/SiC composites

The final average cutting force  $F_s$  is a combination of the total average cutting force at the three cutting stages, which can be obtained by the following expression:

$$\{F_s\} = \frac{\{I_1\}\{F_1\} + \{I_2\}\{F_2\} + \{I_3\}\{F_3\}}{\{I_c\}}$$

(56)

The total theoretical removal volume rate of a single diamond in the grinding process, denoted as  $V_s$ , depends on the amount of interference between the diamond and workpiece at stage I and stage II and the propagation of transverse cracks at stage III;  $V_s$  can be expressed as follows:

$$\{V_s\} = \{I_1\}h_{\{ga1\}}^2 \tan \theta + \{I_2\}h_{\{ga2\}}^2 \tan \theta + 2\{I_3\}C_h C_l$$

(57)

The total material removal volume rate in a rotation period, denoted as  $V_m$ , can be expressed as follows:

$$\{V_m\} = \{I_c\}\{h_m\}\{h_{gm}\}$$

(58)

Therefore, the number of theoretical contact diamond grains between the tool and workpiece in the grinding process, denoted as  $C_a$ , can be expressed as follows:

$$\{C_a\} = \frac{\{V_m\}}{\{V_s\}} = \frac{3\{h_m\}\{h_{gm}\}\{I_c\}}{\{h_{gc}\}^2 \tan \theta (\{I_1\} + \{I_2\}) + 6\{C_h\}\{C_l\}\{I_3\})}$$

(59)

However, the random distribution of diamond grains and the overlap and interference of different diamond grains will affect the total material removal volume and cutting force. Therefore, the correction coefficient  $\lambda$  is introduced. The final theoretical cutting force in the grinding process is given as follows:

$$\{F_p\} = \lambda \{C_a\} \{F_s\} = \frac{3\lambda \{h_m\}\{h_{gm}\} \left( \{I_1\}\{F_1\} + \{I_2\}\{F_2\} + \{I_3\}\{F_3\} \right)}{\{h_{gc}\}^2 \tan \theta (\{I_1\} + \{I_2\}) + 6\{C_h\}\{C_l\}\{I_3\}}$$

(60)

Substituting Eqs. (39), (49), (55), and (59) into Eq. (60), the final theoretical cutting force  $F_p$  is given as follows:

$$\{F_p\} = \frac{\lambda \{h_m\}\{h_{gm}\}H}{\left[ 0.333h_{gc}^2(l_1)C_h + 0.298h_{gc}^2(l_2)C_h + 0.684\sqrt{C_h^2 + C_l^2} \left( h_{gm}^2(l_c) - h_{gc}^2(l_c) \right) \right] \left[ \sqrt{3}h_{gc}^2(l_1 + l_2) + 6C_hC_l(l_3) \right]} \quad (61)$$

(61)

## 4. Experimental Design And Discussions

### 4.1. Experimental setup

The experimental system is shown in Fig. 7. The system consists of data acquisition, machining, and operating systems. The experiment was conducted on a machining center (JDGR200\_A10H, Jingdiao, China). The cutting analogue signals were measured using a dynamometer (9527B, Kistler, Switzerland) and amplified with a charge amplifier (5070A, Kistler). Then, these signals will be transformed into digital signals by an A/D converter (5697A, Kistler) and handled by Dynoware software. The SiC<sub>f</sub>/SiC composites specimen with dimension of 70 mm (length) × 25 mm (width) × 3mm (height) was fixed using a custom fixture. The grinding tool was prepared by a vacuum brazing process. The tool diameter is 6mm, and the mesh number is 80.

### 4.2. Obtaining correction coefficient $\lambda$

According to Eq. (61), the correction coefficient  $\lambda$  can be written as follows:

$$\lambda = \frac{\{F_m\}C_h}{\left[ \sqrt{3}h_{gc}^2(l_1 + l_2) + 6l_3(C_hC_l) \right]} \quad (62)$$

$$\left\{ \frac{\{h_m\}\{h_{gm}\}H}{\left[ 0.333h_{gc}^2(l_1)C_h + 0.298h_{gc}^2(l_2)C_h + 0.684\sqrt{C_h^2 + C_l^2} \left( h_{gm}^2(l_c) - h_{gc}^2(l_c) \right) \right]} \right\}$$

The value of  $\lambda$  can be obtained by experimentation, and then, the final cutting force model can be expressed. The experiments involve three groups of input parameters (spindle speed  $n$ , feed rate  $v_f$  and cutting width  $a_e$ ). The cutting parameters for obtaining  $\lambda$  are listed in Table 3.

Table 3  
Cutting parameters for obtaining  $\lambda$ .

| Group | Spindle speed (rpm)      | Feed rate (mm/min) | Cutting width (um) |
|-------|--------------------------|--------------------|--------------------|
| 1     | 2500,3500,4500,5500,6500 | 50                 | 48                 |
| 2     | 4500                     | 20,35,50,65,80     | 48                 |
| 3     | 4500                     | 50                 | 16,32,48,64,80     |

Each group of parameters was tested three times to reduce the error. The experimental force at the stable stage was determined, and the resultant force  $F_m$ ,  $F_m=(F_x+F_y)^{1/2}$  was obtained. The correction coefficient  $\lambda$  was calculated by substituting the resultant force into Eq. (62), and the final results are shown in Fig. 8.

The value of the correction coefficient showed minimal change with the change of different input variables. Therefore, the three-stage average parameter is selected, and the final average value of the correction parameter  $\lambda$  is 0.186. Therefore, the final theoretical average cutting force  $F_p$  can be expressed as follows:

$$\{F_p\}=\frac{0.186\{h_m\}\{h_{gm}\}}{H}\left[0.333h_{gc}^2(l_1)C_h+0.298h_{gc}^2(l_2)C_h+0.684\sqrt{C_h^2+C_l^2}\left(h_{gm}^2(l_c)-h_{gc}^2(l_c)\left(\frac{l_1+l_2}{l_1+l_2}\right)\right)\right]\{(C_h)\left[1.73h_{gc}^2\left(\frac{l_1+l_2}{l_1+l_2}\right)+6(C_h)C_l(l_3)\right]\}$$

(63)

### 4.3. Verifying the model and discussions

The cutting force  $F_p$  calculated by the model was compared with the cutting force  $F_m$  measured in the experiment to verify the accuracy of the cutting force model. The experimental parameters are listed in Table 4.

Table 4  
Cutting parameters for milling experiments.

| Group | Spindle speed (rpm)      | Feed rate (mm/min) | Cutting width (um) |
|-------|--------------------------|--------------------|--------------------|
| 1     | 3000,3600,4200,4800,5400 | 60                 | 30                 |
| 2     | 3600                     | 24,36,48,60,72     | 30                 |
| 3     | 3600                     | 60                 | 20,30,40,50,60     |

Five gradients were set for each parameter of the experiment. Each experiment was repeated three times to reduce error. A comparison between the cutting force measured in the experiment and the cutting force calculated by the model is shown in Fig. 9; as shown, their changing trend and value are in good agreement.

In addition, the cutting force model was used to predict the cutting force with different input variables to better understand the influencing factors of the cutting force of side grinding of orthogonal laminated SiC<sub>f</sub>/SiC composites. The predicted relationship between the cutting force and input variables is shown in Fig. 10.

Figure 10(a) shows the influence of the spindle speed on the cutting force. When the cutting width and feed rate are constant, the cutting force decreases with increasing spindle speed because when the material with a given volume is removed, more diamond grains will participate in the grinding process as the spindle speed increases. The cutting time will decrease, and the depth of engagement between the

diamond grains and workpiece will become smaller. Moreover, the maximum undeformed chip thickness of a single diamond grain is reduced, resulting in a decrease in material removal in the brittle region, thus reducing the cutting force of each grain. Higher cutting speeds will reduce the probability of continuous cracking and fracture density, increase flow toughness, and reduce strength degradation. Therefore, the final cutting force will be reduced, consistent with the trend of the experimental results.

Figure 10(b) shows the influence of feed rate on the cutting force. When the spindle speed and cutting width are constant, the cutting force increases as the feed rate increases, consistent with the experimental result because more diamond grains are involved in the grinding process at lower feed rate, resulting in lower engagement depth between the diamond grains and workpiece. The cracks gradually form and spread from stage II, which may take time depending on the local stress concentration. After the crack has formed and propagated, the tensile stress concentration decreases, and the crack cannot nucleate until the next tensile stress concentration is established. Therefore, tensile stress in the workpiece will continue to accumulate at low feed rate, resulting in a high possibility of continuous cracking and crack interaction. The reduced removal rate leads to a reduction in the undeformed chip thickness, resulting in more plastic flow and less brittle fracture and reducing the cutting force.

Figure 10(c) shows the influence of cutting width on the cutting force. When the spindle speed and feed rate are constant, the cutting force increases with the increase of cutting width because when the cutting width increases, the contact area between the tool and workpiece expands, leading to more diamond grains participating in the grinding process. The tool may be partially deformed when subjected to greater cutting force, thus resulting in a longer actual contact length than the theoretical length. Moreover, the cutting proportion of the brittle region increases as the cutting width increases, which will increase the cutting force. The predicted result is consistent with the experimental result.

In this model, the effective elastic constants of orthogonal laminated SiC<sub>f</sub>/SiC composites are idealized and calculated, but some deviations may occur due to different processes and stability in actual production. Concurrently, some diamond grains wear may occur in the actual grinding process, possibly causing the actual cutting force to be greater than the predicted cutting force. The limitations may have some impact on the results.

Analytical modeling of side grinding of orthogonal laminated SiC<sub>f</sub>/SiC composites is a complex process because of the random size, shape, and arrangement of the diamond grains on the tool surface. In addition, the apparent anisotropy of SiC<sub>f</sub>/SiC creates a more complex structure than that of other isotropic homogeneous materials. In this study, the corresponding idealized analysis of laminated SiC<sub>f</sub>/SiC composites is performed, and the cutting force model of side grinding is established. The predicted data are in good agreement with the experiment. Results indicate that the macromechanical analysis is an effective method for studying the effective elastic properties of orthogonal laminated SiC<sub>f</sub>/SiC composites. The model found that the cutting force was lower at a high spindle speed, low feed rate, and small cutting width. Moreover, the cutting force value presents a non-linear decreasing trend with increasing spindle speed but increases linearly with increasing feed rate and cutting width. The

spindle speed and cutting width have more influence on the cutting force than the feed rate. The model can adequately evaluate the effective elastic properties of orthogonal laminated SiC<sub>f</sub>/SiC composites and effectively improve the machining efficiency while ensuring machining quality in future applications.

## 5. Conclusions

In this study, the effective elastic properties of orthogonal laminated SiC<sub>f</sub>/SiC composites were analysed, and the cutting force model was established with considering three cutting stages. The tangential and normal cutting forces were both considered in the modeling process. Finally, the accuracy of the model was verified by experimentation. The following conclusions were obtained:

1. The fabrication process of laminated composites is complicated and unstable, and the effective elastic constants can be determined through theoretical analysis. For macroscopic mechanical property analyses of orthogonal laminated SiC<sub>f</sub>/SiC composites, the anisotropy between the layers should also be considered.
2. The ductile-to-brittle transition of hard and brittle materials is not an instantaneous value, but an intermediate stage. It can be divided into the ductile stage, ductile-to-brittle transition stage and brittle stage for analysis. The tangential cutting force plays an important role in the grinding process. The interaction between the tool and workpiece is consistent with the microscopic contact between the diamond grains and material.
3. Some deviations may occur due to different processes and stability in actual production of orthogonal laminated SiC<sub>f</sub>/SiC composites. In addition, tool wear may occur in the actual grinding process. The limitations may have some impact on the results. The differences between the predicted and measured data of the cutting force were analysed from the perspectives of the undeformed chip thickness, proportion of brittleness stage, and contact deformation between the tool and workpiece.
4. According to the cutting force model, increasing the spindle speed and decreasing the feed rate and cutting width can reduce the cutting force. The cutting force value presents a non-linear decreasing trend with increasing spindle speed but increases linearly with increasing feed rate and cutting width. The spindle speed and cutting width have more influence on the cutting force than the feed rate.
5. Under different combinations of input variables (spindle speed, feed rate, cutting width), the predicted value is in good agreement with the experimental value, and the average error is 7.43%. The modeling process can be applied to evaluate the effective elastic properties of orthogonal laminated SiC<sub>f</sub>/SiC composites, and predict the cutting force. The model can be used to effectively evaluate grinding processes and improve the machining efficiency in future applications.

## Declarations

**Author contribution** Zikang Zhang: methodology, experiments, writing-original draft, writing-review and editing; Songmei Yuan: funding acquisition, writing-review and editing; Xiaoxing Gao and Weiwei Xu:

supervision; Jiaqi Zhang and Wenzhao An: experiments.

**Funding** This work is supported by the National Science and Technology Major Project of China (2017-VII-0015-0111).

**Data Availability** All data generated or analyzed during this study are included in this article.

**Ethics approval** Not applicable.

**Consent to participate** Not applicable.

**Consent for publication** Not applicable.

**Competing interests** The authors declare no competing interests.

## References

1. Wang Y, Sarin VK, Lin B et al (2016) Feasibility study of the ultrasonic vibration filing of carbon fiber reinforced silicon carbide composites. *Int J Mach Tools Manuf* 101:10–17.  
<https://doi.org/10.1016/j.ijmachtools.2015.11.003>
2. Qu S, Gong Y, Yang Y et al (2020) Mechanical model and removal mechanism of unidirectional carbon fibre-reinforced ceramic composites. *Int J Mech Sci* 173.  
<https://doi.org/10.1016/j.ijmecsci.2020.105465>
3. Hu Y, Shi D, Hu Y et al (2019) Experimental investigation on the ultrasonically assisted single-sided lapping of monocrystalline SiC substrate. *J Manuf Process* 44:299–308.  
<https://doi.org/10.1016/j.jmapro.2019.06.008>
4. Gong Y, Qu S, Yang Y et al (2019) Some observations in grinding SiC and silicon carbide ceramic matrix composite material. *Int J Adv Manuf Technol* 103:3175–3186.  
<https://doi.org/10.1007/s00170-019-03735-w>
5. Cao J, Wu Y, Li J, Zhang Q (2015) A grinding force model for ultrasonic assisted internal grinding (UAIG) of SiC ceramics. *Int J Adv Manuf Technol* 81:875–885. <https://doi.org/10.1007/s00170-015-7282-0>
6. Yin J, Xu J, Ding W, Su H (2021) Effects of grinding speed on the material removal mechanism in single grain grinding of SiCf/SiC ceramic matrix composite. *Ceram Int* 47:12795–12802.  
<https://doi.org/10.1016/j.ceramint.2021.01.140>
7. Dong X, Shin YC (2017) Improved machinability of SiC/SiC ceramic matrix composite via laser-assisted micromachining. *Int J Adv Manuf Technol* 90:731–739. <https://doi.org/10.1007/s00170-016-9415-5>
8. Gavalda Diaz O, Axinte DA, Butler-Smith P, Novovic D (2019) On understanding the microstructure of SiC/SiC Ceramic Matrix Composites (CMCs) after a material removal process. *Mater Sci Eng A* 743:1–11. <https://doi.org/10.1016/j.msea.2018.11.037>

9. Qu S, Gong Y, Yang Y et al (2019) Grinding characteristics and removal mechanism of 2.5D-needed Cf/SiC composites. *Ceram Int* 45:21608–21617. <https://doi.org/10.1016/j.ceramint.2019.07.156>
10. Mir A, Luo X, Sun J (2016) The investigation of influence of tool wear on ductile to brittle transition in single point diamond turning of silicon. *Wear* 364–365:233–243. <https://doi.org/10.1016/j.wear.2016.08.003>
11. Rao X, Zhang F, Luo X et al (2019) Material removal mode and friction behaviour of RB-SiC ceramics during scratching at elevated temperatures. *J Eur Ceram Soc* 39:3534–3545. <https://doi.org/10.1016/j.jeurceramsoc.2019.05.015>
12. Pratap A, Patra K (2020) Evolution of chemo-mechanical effects during single grit diamond scratching of monocrystalline silicon in the presence of potassium hydroxide. *Wear* 452–453:203292. <https://doi.org/10.1016/j.wear.2020.203292>
13. Dai J, Su H, Yu T et al (2018) Experimental investigation on materials removal mechanism during grinding silicon carbide ceramics with single diamond grain. *Precis Eng* 51:271–279. <https://doi.org/10.1016/j.precisioneng.2017.08.019>
14. Hwang TW, Malkin S (1999) Grinding mechanisms and energy balance for ceramics. *J Manuf Sci Eng Trans ASME* 121:623–631. <https://doi.org/10.1115/1.2833081>
15. Malkin S, Hwang TW (1996) Grinding Mechanisms for Ceramics. *CIRP Ann - Manuf Technol* 45:569–580. [https://doi.org/10.1016/S0007-8506\(07\)60511-3](https://doi.org/10.1016/S0007-8506(07)60511-3)
16. Cheng J, Yu T, Wu J, Jin Y (2018) Experimental study on “ductile-brittle” transition in micro-grinding of single crystal sapphire. *Int J Adv Manuf Technol* 98:3229–3249. <https://doi.org/10.1007/s00170-018-2503-y>
17. Xiao X, Zheng K, Liao W, Meng H (2016) Study on cutting force model in ultrasonic vibration assisted side grinding of zirconia ceramics. *Int J Mach Tools Manuf* 104:58–67. <https://doi.org/10.1016/j.ijmachtools.2016.01.004>
18. Kar S, Kumar S, Bandyopadhyay PP, Paul S (2020) Grinding of hard and brittle ceramic coatings: Force analysis. *J Eur Ceram Soc* 40:1453–1461. <https://doi.org/10.1016/j.jeurceramsoc.2019.12.058>
19. Wang J, Zhang J, Feng P (2017) Effects of tool vibration on fiber fracture in rotary ultrasonic machining of C/SiC ceramic matrix composites. *Compos Part B Eng* 129:233–242. <https://doi.org/10.1016/j.compositesb.2017.07.081>
20. Zhang L, Wang S, Li Z et al (2019) Influence Factors on Grinding Force in Surface Grinding of Unidirectional C/SiC Composites. *Appl Compos Mater* 26:1073–1085. <https://doi.org/10.1007/s10443-019-09767-5>
21. Ning F, Cong W, Wang H et al (2017) Surface grinding of CFRP composites with rotary ultrasonic machining: a mechanistic model on cutting force in the feed direction. *Int J Adv Manuf Technol* 92:1217–1229. <https://doi.org/10.1007/s00170-017-0149-9>
22. Wang H, Hu Y, Cong W, Hu Z (2019) A mechanistic model on feeding-directional cutting force in surface grinding of CFRP composites using rotary ultrasonic machining with horizontal ultrasonic

- vibration. *Int J Mech Sci* 155:450–460. <https://doi.org/10.1016/j.ijmecsci.2019.03.009>
23. Han Q, Wang J, Han Z et al (2021) An effective model for mechanical properties of nacre-inspired continuous fiber-reinforced laminated composites. *Mech Adv Mater Struct* 28:1849–1857. <https://doi.org/10.1080/15376494.2020.1712626>
24. Takeda T (2018) Micromechanics model for three-dimensional effective elastic properties of composite laminates with ply wrinkles. *Compos Struct* 189:419–427. <https://doi.org/10.1016/j.compstruct.2017.10.086>
25. Hsiao HM, Daniel IM (1996) Effect of fiber waviness on stiffness and strength reduction of unidirectional composites under compressive loading. *Compos Sci Technol* 56:581–593. [https://doi.org/10.1016/0266-3538\(96\)00045-0](https://doi.org/10.1016/0266-3538(96)00045-0)
26. Chen M, Zhao Q, Dong S, Li D (2005) The critical conditions of brittle-ductile transition and the factors influencing the surface quality of brittle materials in ultra-precision grinding. *J Mater Process Technol* 168:75–82. <https://doi.org/10.1016/j.jmatprotec.2004.11.002>
27. Zhang X, Kang Z, Li S et al (2019) Grinding force modelling for ductile-brittle transition in laser macro-micro-structured grinding of zirconia ceramics. *Ceram Int* 45:18487–18500. <https://doi.org/10.1016/j.ceramint.2019.06.067>
28. Lawn BR, Evans AG, D.B.Marshall (1980) Elastic / Plastic Indentation Damage in Ceramics: The MediadRadial Crack System. *J Am Ceram Soc* 63:574–581. <https://doi.org/10.1111/j.1151-2916.1980.tb10768.x>
29. Yang M, Li C, Zhang Y et al (2017) Maximum undeformed equivalent chip thickness for ductile-brittle transition of zirconia ceramics under different lubrication conditions. *Int J Mach Tools Manuf* 122:55–65. <https://doi.org/10.1016/j.ijmachtools.2017.06.003>
30. Agarwal S, Rao PV (2013) Predictive modeling of force and power based on a new analytical undeformed chip thickness model in ceramic grinding. *Int J Mach Tools Manuf* 65:68–78. <https://doi.org/10.1016/j.ijmachtools.2012.10.006>
31. Xu HHK, Jahanmir S, Ives LK (1997) Effect of grinding on strength of tetragonal zirconia and zirconia-toughened alumina. *Mach Sci Technol* 1:49–66. <https://doi.org/10.1080/10940349708945637>
32. Zhang F, Meng B, Geng Y et al (2016) Friction behavior in nanoscratching of reaction bonded silicon carbide ceramic with Berkovich and sphere indenters. *Tribol Int* 97:21–30. <https://doi.org/10.1016/j.triboint.2016.01.013>
33. Shi H, Yuan S, Zhang C et al (2020) A cutting force prediction model for rotary ultrasonic side grinding of CFRP composites considering coexistence of brittleness and ductility. *Int J Adv Manuf Technol* 106:2403–2414. <https://doi.org/10.1007/s00170-019-04730-x>
34. Li Z, Zhang F, Luo X et al (2018) A new grinding force model for micro grinding RB-SiC ceramic with grinding wheel topography as an input. *Micromachines* 9. <https://doi.org/10.3390/mi9080368>

## Figures



**Figure 1**

The illustrations on (a) the structure of orthogonal laminated SiC<sub>f</sub>/SiC composites, (b) SiC<sub>f</sub>/SiC monolayer composite material.

## **Figure 2**

Laminated SiC<sub>f</sub>/SiC composites: (a) global view, (b) the relationship between fibre orientation and material coordinate system, and (c)  $x_m$ - $z_m$  cross-section.

## **Figure 3**

The illustrations on (a) side grinding, (b) octahedral diamond grain.

## **Figure 4**

The illustrations on (a) randomly protruding height of diamond grains, (b) the plane expansion of diamond grains, (c) average protrusion height of diamond grains, (d) the plane expansion of the average protrusion height of diamond grains.

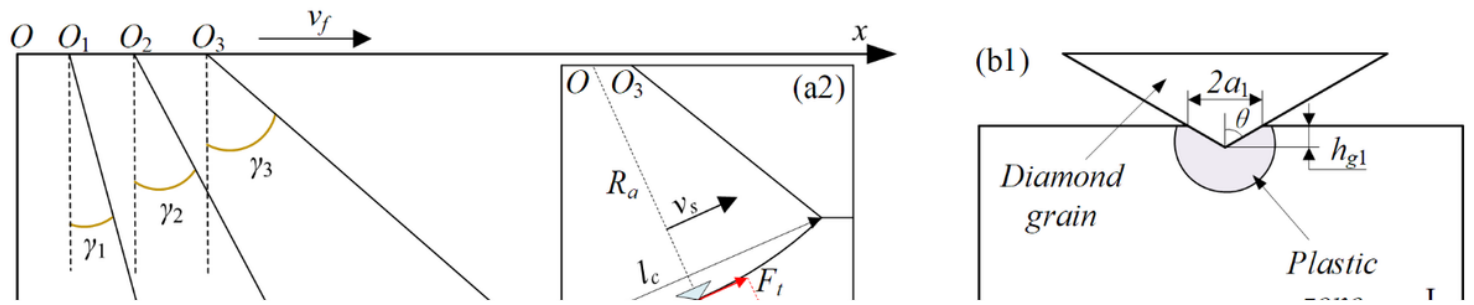


**Figure 5**

The illustrations on (a) cutting mechanism of a single diamond grain, (b) three cutting stages.

**Figure 6**

The grinding process of a single diamond grain.

**Figure 7**

Experimental setup.

## **Figure 8**

Influences of input variables on the correction coefficient  $\lambda$ .

## **Figure 9**

Comparison of experimental and theoretical cutting force values.

## **Figure 10**

The relationship between the predicted cutting force values and input variables.